




A mineralogical and isotopic study of the historic monomict eucrite Padvarninkai

T. J. BARRETT ^{1,2*}, A. J. KING ^{1,3}, G. DEGLI-ALESSANDRINI¹, S. J. HAMMOND⁴,
E. HUMPHREYS-WILLIAMS³, B. SCHMIDT³, R. C. GREENWOOD¹, F. A. J. ABERNETHY ¹,
M. ANAND^{1,3}, and E. RUDNICKAITĖ⁵

¹School of Physical Sciences, The Open University, Milton Keynes, UK

²Center for Lunar Science and Exploration, Lunar and Planetary Institute, Houston, Texas, USA

³Planetary Materials Group, Natural History Museum, London, UK

⁴School of Environment, Earth, and Ecosystem Sciences, The Open University, Milton Keynes, UK

⁵Department of Geology and Mineralogy, Museum of Geology of Vilnius University, Vilnius, Lithuania

*Correspondence

T. J. Barrett, School of Physical Sciences, The Open University, Walton Hall, Milton Keynes MK7 6AA, UK.
Email: tbarrett@lpi.usra.edu

(Received 24 May 2023; revision accepted 02 June 2024)

Abstract—The Padvarninkai meteorite is a relatively understudied eucrite, initially misclassified as a shergottite given its strong shock characteristics. In this study, a comprehensive examination of the petrology; mineral composition; major, minor, and trace element abundances; and isotopic composition (C, O) is presented. Padvarninkai is a monomict eucrite consisting of a fine to coarse-grained lithology and impact melt veins. Pyroxene grains are typically severely fractured and mosaicked whilst plagioclase is either partially or totally converted to maskelynite. Based on shock features observed in pyroxene, plagioclase, and apatite, Padvarninkai can be given a shock classification of M-S4/5. Despite the high shock experienced by this sample, some of the original igneous textures remain. Compositionally, Padvarninkai is a main group eucrite with a flat REE pattern ($\sim 10\text{--}12\times\text{CI}$) and elevated Ni abundances. Whilst both new and literature oxygen isotopes are similar to other eucrites, however, Padvarninkai displays an anomalously high $\delta^{13}\text{C}$ value. To reconcile the high Ni and $\delta^{13}\text{C}$ value, impact contamination modeling was conducted. These models could not reconcile both the high Ni and $\delta^{13}\text{C}$ value with the eucritic $\delta^{18}\text{O}$ values, arguing against impact as a source for these anomalies.

INTRODUCTION

Eucrites are differentiated achondrites which share a common provenance with howardites and diogenites to form the HED meteorites. The HED meteorites constitute the largest group of achondrites available from a differentiated asteroid, likely 4 Vesta (e.g., De Sanctis et al., 2012; McSween et al., 2013). As such, samples from this group can provide unparalleled insight into the differentiation processes that occurred on proto-planetary bodies early in Solar System history.

The eucrites themselves are plagioclase, pigeonite-bearing basaltic achondrites (Duke & Silver, 1967) and make up the largest portion of the HEDs ($\sim 63\%$;

Meteoritical Bulletin <http://www.lpi.usra.edu/meteor/metbull.php>; accessed 25 September 2023). The eucrites have magmatic textures and chemical compositions indicating formation as basaltic lavas or intrusions and, hence, are regarded as samples from the outer crustal layers of their parent body (Barrat et al., 2007; De Sanctis et al., 2012, 2013). Based on their petrographic and chemical characteristics, monomict and unbrecciated eucrites are subdivided into basaltic and cumulate groups with basaltic eucrites being further subdivided into Main Group-Nuevo Laredo (hereafter referred to as Main Group) and Stannern trend based on their Mg# ($\text{Mg}/[\text{Mg} + \text{Fe}]$), Ti, and incompatible trace elements (B.V.S.P., 1981; Barrat et al., 2000, 2007; Mayne et al.,

2009). A third geochemical trend dubbed the residual eucrites was observed by Yamaguchi et al. (2009) and is believed to be the light rare earth element (REE)-depleted residuum left by partial melts that contaminated regular eucrites and consequently created the Stannern trend (Barrat et al., 2007).

The Padvarninkai (a.k.a. Andrionishkis [En] or Andrioniškis [Lt]) meteorite fell in Lithuania on February 9, 1929 with over 100 eyewitness accounts placing the time of the fall at $00:45 \pm 00:05$ CET. The sample was originally classified as a shergottite by Binns (1967) owing to the presence of maskelynite. Mason et al. (1979), however, demonstrated its chemical composition to be identical to eucrites, with further confirmation by Greenwood et al. (2005) through oxygen isotope analysis. Given its strong shock features, it is believed that Padvarninkai is the most shocked eucrite (Yamaguchi et al., 1993), and based on the scale of Bischoff and Stöffler (1992) the equilibrium shock pressure was estimated to be between ~ 42 and 60 GPa (S5). The weighted mean $^{207}\text{Pb}/^{206}\text{Pb}$ age as recorded by zircon and baddeleyite is approximately 4553 ± 13 Ma and is believed to record primary crystallization (Bukovanská et al., 1997; Misawa et al., 2005).

Currently, much of the published data for Padvarninkai focuses more on the age dating (Bukovanská et al., 1997; Kunz et al., 1997) with some data regarding data on its petrology or bulk composition (Barrat et al., 2000; Mason et al., 1979; Miyahara et al., 2021; Urey & Craig, 1953). Given Padvarninkai is a witnessed fall, suggesting minimal time for terrestrial alteration, as well as one of, if not the, most shocked eucrite currently known within the meteorite collection, closer investigation of this sample could provide insight into the eucrites as well as how shock affects them. In this study, a comprehensive examination of the petrology; mineral composition; bulk-rock major, minor, and trace element abundances; and bulk-rock isotopic composition (C, O) is presented to provide a foundation for further work on this eucrite. Alongside Padvarninkai, the first data for Dar al Gani (DAG) 844 are provided for comparative purposes.

SAMPLES AND METHODS

Two polished thin sections were prepared at The Open University from an 18.95 g piece of Padvarninkai provided by Vilnius University Department of Geology and Mineralogy, as well as a polished thin section from the Smithsonian Institute (USNM 5946).

Scanning Electron Microscopy

Each polished thin section was carbon-coated using an EMITECH K950X Turbo carbon sputter coater and examined at The Open University using a FEI Quanta

Scanning Electron Microscope (SEM) fitted with an Oxford Instrument X-Max 80mm² Energy Dispersive X-ray detector. An electron beam with an acceleration voltage of 20 kV and a beam current of 0.6 nA was used for the acquisition of all the backscattered electron (BSE) images and X-ray chemical maps.

Modal abundances were calculated using the pixel histograms in the free software ImageJ[®] on 77 high-quality BSE images (1024 pixels, ~ 200 –500 magnification, dwell time 10 μs ; Smithsonian section $n=27$; other sections $n=25$ each for a total area of ~ 31.33 mm²). The modal mineralogy of each section and the average abundance for each phase are given in Table 1.

Raman Spectroscopy

Raman spectroscopy was performed on a selection of silica grains in all three thin sections. The analyses were conducted using a Horiba Jobin-Yvon LabRAM HR Raman microscope with a $\times 100$ long working distance objective and a 514.5 nm laser operating at between 1.25 and 2.5 mW with a 600 grooves per mm grating. Hole and slit settings were 300 and 150, respectively. Collection times varied from 10 to 60 s depending on the response from the grain and 5–15 acquisitions were performed to improve signal to noise ratio. Spectra were collected in the range of 100–1600 cm^{-1} with significant interference at the higher end of this range caused by the pre-existing carbon coat which was subsequently cut. The spectra at the lower end were compared to reference spectra from the RRUFF database (R040031 and R090042 for quartz and tridymite, respectively).

Electron Probe Microanalysis

Major silicate minerals were analyzed using wavelength-dispersive X-ray spectroscopy conducted on the Cameca SX100 electron microprobe at The Open University. Beam conditions included an accelerating voltage of 20 kV and a beam current of 20 nA with a 10 μm spot size. The following crystals were used for the analysis: TAP (Si, Mg), LTAP (Na, Al), LLIF (Mn, Fe, Cr), LPET (K, Ti), and PET (Ca), using a ZAF correction. The elements of interest were calibrated against in-house EPMA standards: for pyroxene, diopside (Ca, Mg, Si), kaersutite (Al), rutile (Ti), rhodonite (Mn), and fayalite (Fe); for plagioclase, anorthite glass (Si, Al, Ca), oligoclase (Na), kaersutite (Mg), orthoclase (K); for chromite, ilmenite, and oxides: chromite (Al, Cr, Fe, Mg), diopside (Ca, Si), rutile (Ti), vanadium metal (V), and rhodonite (Mn).

For apatite analyses, the beam conditions used to measure volatiles were similar to those recommended by Goldoff et al. (2012) (10 kV, 4 nA) to minimize the potential mobilization of volatile elements. These settings

TABLE 1. Modal abundance (vol%) for each thin section of Padvarninkai and their total average. The number of “frames” refers to the number of individual images used to calculate the modal abundance.

Thin section	Frames	Total area (mm ²)	Low-Ca Pyroxene	High-Ca pyroxene	Plagioclase	Silica	Oxide	Melt	Sum
Smithsonian	27	5.299	32.5	10.1	47.8	7.1	1.5	1.0	100
Vilnius #1	25	13.017	33.2	14.9	35.3	14.0	2.6	0.0	100
Vilnius #2	25	13.017	37.4	10.3	38.0	12.0	2.3	0.0	100
Total	77	31.334	34.3	11.7	40.6	10.9	2.1	0.3	100

have been previously used at the Open University to analyze apatite (e.g., Barrett et al., 2019). The spot size used for analyses was 5 μm .

To minimize the mobilization of volatiles, F and Cl were measured first on PCO and LPET crystals, respectively, along with Ca and P under the “light” analytical conditions (10 kV, 4 nA). The crystals were then rotated out of position and the remaining elements were analyzed together under the same beam conditions as the silicate minerals (20 kV, 20 nA).

Calibration standards used for these analyses include: apatite (Ca, F, P), barite (S), bustamite (Mn), forsterite (Mg, Fe), monazite (Ce), plagioclase (Na, Si), strontium fluoride (F), sylvite (Cl), yttrium phosphate (Y). A secondary apatite standard was analyzed prior to analyzing unknowns and compared to its known chemical composition to ascertain precision and reproducibility (accuracy better than 0.91 wt% 2σ for all elements; reproducibility better than 0.85 wt% 2σ for all elements; integrated across all analysis sessions).

Analysis of DaG 844 major silicates (see supplementary material) was conducted using the Cameca SX100 at the NASA Johnson Space Center. Beam conditions included an accelerating voltage of 20 kV, and a beam current of 40 nA for pyroxene. These beam conditions and the counting times used are those of Mittlefehldt (2005) and result in greater precision of Fe/Mn ratios than commonly used EPMA protocols. Plagioclase was analyzed with a 15 kV, 20 nA beam, and 3 μm spot size. The elements of interest were calibrated against in-house EPMA standards: for pyroxene, diopside (Ca, Mg, Si), kaersutite (Al), rutile (Ti), rhodonite (Mn), and fayalite (Fe); for plagioclase, anorthite glass (Si, Al, Ca), oligoclase (Na), kaersutite (Mg), orthoclase (K).

X-Ray Diffraction

Three distinct powdered fractions were scraped using clean tools from surface of the large Padvarninkai hand specimen provided for the current study: TJB-001 a region on the surface that appeared rusted, TJB-002 the orange-stained region, and TJB-003 fresh Padvarninkai material (Figure 1). The mineralogy of powdered samples was characterized using a PANalytical X’Pert Pro

scanning X-ray diffractometer (XRD) at the Natural History Museum (NHM), London. Approximately 1 mg of each powder was mixed with several drops of acetone and prepared as a thin smear on a zero-background substrate. XRD patterns were then collected for each sample from 20 to 65° (2 θ , with a step size of 0.02°) in reflection geometry using Co-K α radiation ($\lambda = 1.789 \text{ \AA}$). Mineral phases in the samples were identified using the International Centre for Diffraction Data (ICDD) database (PDF-2). Detection limits for XRD analyses are ~ 1 wt%, depending on the phase.

XRD patterns of the different scrapings of Padvarninkai are shown in Figure S5.

Thermogravimetric Analysis (TGA)

Approximately 7 mg aliquots, from the same reservoirs used for XRD (except TJB-001, which was ~ 0.5 mg), were characterized using a TA Instruments Simultaneous Thermal Analysis (SDT) Q600 at the NHM. The powders were loaded into an alumina crucible, placed onto the TGA balance, and then sealed within the furnace. The mass of each sample was recorded as it was heated from room temperature to 1000°C at 10°C min⁻¹ under a N₂ flow of 100 mL min⁻¹.

TGA combustion profiles are shown in Figure S6.

Bulk-Rock Major, Minor, and Trace Element Analyses

The major, minor, and trace element composition of the meteorites DaG 844 and Padvarninkai were determined using inductively coupled plasma optical emission spectroscopy (ICP-OES) and inductively coupled plasma mass spectrometry (ICP-MS) in the Imaging and Analysis Centre (IAC) at the NHM.

A chip of each meteorite (~ 1 g) was powdered in a clean laboratory at The Open University using an agate mortar and pestle. Approximately 40 mg of the powder was pre-treated with 0.5 mL of concentrated HNO₃ and fused with 120 mg of LiBO₂ in a Pt/Au crucible. The resulting quenched material was subsequently dissolved in 1.56 M HNO₃ and made up to a final concentration of 0.62 M HNO₃. Major element abundances were



FIGURE 1. Hand specimen photographs of a piece of Padvarninkai. (Color figure can be viewed at [wileyonlinelibrary.com](https://onlinelibrary.wiley.com/doi/10.1111/mpe.14229))

determined, in triplicate, using a Thermo iCap 6500 Duo ICP-OES instrument. The instrument was calibrated using a range of certified reference materials (CRMs), which were prepared in the same way. The CRMs BHVO-2 (basalt) and JG-1 (granodiorite) were analyzed to monitor accuracy.

Minor and trace element abundances were determined on a separate aliquot of powdered meteorites. Approximately 40 mg of the powder was digested in HF + HClO₄ + HNO₃ + H₂O₂ before analysis in triplicate using an Agilent 8900 ICP-MS/MS instrument. Non-isobaric interferences were reduced by tuning CeO⁺/Ce⁺ and Ba⁺⁺/Ba⁺ to <1%; for As, Zn, Eu, Gd, Tb, Dy, Er, and Hf corrections were applied for polyatomic and doubly charged interferences from Nd & Sm⁺⁺, Ti, Ba, Ce & Pr, Nd, Dy, Sm, and Nd & Sm, respectively. No gas and He mode were used for differing elements dependent on the agreement with the CRMs. The accuracy of the trace element analyses was monitored using the CRMs BCR-2 (basalt), GSP-2 (granodiorite), HG-1 (granodiorite), and SY-2 (syenite). The limit of quantification, one standard deviation on three replicates, and measured standard data are provided in the [supplementary material](#).

In addition, bulk minor and trace element abundances were also determined on a separate aliquot of powder of Padvarninkai at the Open University. Approximately 25 mg of powder was digested in HF and HNO₃ (4:1 ratio) at 120°. Following this, the sample was dried, and HCl was added to remove any remaining fluorides. The sample was again dried down, converted to HNO₃, and diluted to exactly 1000-fold dilution of the original powder weight in a 2% HNO₃ solution. Samples were analyzed using an Agilent 8800 ICP-MS/MS instrument, using no gas, He (collision), or O₂ (mass shifted reaction) mode in the collision cell. Doubly charged generation was assessed during tuning using Ce⁺⁺/Ce⁺ (1.64% in no gas mode, and 1.53% in He mode) and oxide generation by using CeO⁺/Ce⁺ (1.05% in no gas mode, and 0.54% in He

mode). The REEs were analyzed using O₂ mode (mass shifted). Other elements are reported in either no gas or He mode (see supplementary data for exact list), depending on agreement with the CRM, detection limits, and potential interferences. An online internal standard (be, In, Rh, Tm, Re, Bi) was used to monitor any instrument drift throughout the run. No drift correction was necessary. Data were calibrated using BIR-1, W-2, DNC-1, BHVO-2, and AGV-1. The accuracy of the analysis of Padvarninkai is assessed primarily using a separate digest of BHVO-2 (and to a lesser extent JP-1), digested at the same time as the sample and at approximately the same sample mass (see supplementary data for more details). A total procedural blank has also been reported, factoring in both chemistry and instrumental blank contributions. Each mass is measured five times per analytical run, the average of these 5 measurements, and the relative standard deviation of these measurements are reported. Detection limits are calculated using Agilent's Mass Hunter software.

Carbon and Nitrogen Isotopes

Padvarninkai was analyzed for its bulk carbon and nitrogen isotopes on the stepped combustion gas extraction mass spectrometry system Finesse at The Open University. Two aliquots of material totaling 16,0301 mg were taken from the main mass of Padvarninkai and wrapped in clean Pt foil and combusted in a stepwise manner in a quartz furnace using oxygen derived from the decomposition of copper oxide. In this case, steps of 100°C were used. At each step, the gas was split between a cold finger and a molecular sieve in order to separate the carbon and nitrogen. Carbon was analyzed on a Chell MK 3934 Baratron for abundance and a triple collector magnetic sector mass spectrometer for isotopes. Nitrogen was measured using a quadrupole (Hiden HAL 3F PIC) and a separate, dual-focusing magnetic sector mass

spectrometer. Full sample preparation and analysis details can be found in Abernethy et al. (2018).

Carbon isotopic analyses are reported in the standard delta (δ) notation, where $\delta^{13}\text{C}$ has been calculated as:

$$\delta^{13}\text{C} = \left\{ \left(\frac{R_{\text{sample}}}{R_{\text{standard}}} \right) - 1 \right\} \times 1000$$

where R is the $^{13}\text{C}/^{12}\text{C}$ ratio and the reference standard is the Vienna Pee Dee Belemnite (VPDB) with a $\delta^{13}\text{C}$ of 0 ‰. Uncertainties for $\delta^{13}\text{C}$ are calculated by error propagation.

Oxygen Isotopic Analysis: Sample Preparation and Analytical Procedures

Similar to many eucrites, Padvarninkai shows evidence of brecciation and the development of shock-melt veins (Mittlefehldt, 2015). The same three distinct fractions used for XRD and TGA (although not from the same aliquots as additional material was required) were separated from Padvarninkai for the current study. To ascertain if the sample contains any terrestrial weathering, a fraction of each of the samples was washed in EATG (ethanolamine thioglycolate) which is known to remove terrestrial weathering products; in particular, Fe-bearing phases such as Fe-hydroxides and oxyhydroxides (Alexander et al., 2018; Greenwood et al., 2012, 2015; Janots et al., 2012; Martins et al., 2007). EATG is preferred over conventional dilute HCl leaching as HCl can partially remove indigenous glass, phosphate, and feldspathic material (Greenwood et al., 2012). Work by Alexander et al. (2018), however, noted that EATG treatment can remove primary components in the case of CO chondrite falls, likely Fe-rich phases in the matrix. As Padvarninkai is a fall, it is unlikely to have undergone significant terrestrial alteration. As a differentiated achondrite with a low metal content, it is also less prone to oxidation in the terrestrial environment than more Fe-rich meteorites. In the absence of metal, it has been demonstrated that terrestrial weathering does not have a significant effect on O isotopes compared to noble gases (Schwenzer et al., 2013), as such EATG leaching on an Fe-poor fall may well remove primary phases (Alexander et al., 2018). In addition to the EATG-washed and non-EATG-washed fractions, replicate analyses from the same powder used in Greenwood et al. (2017) were made.

Oxygen isotopic analysis was undertaken at The Open University using a modified version of the infrared laser-assisted fluorination system described by Miller et al. (1999) and the details of which can be found in Greenwood et al. (2015). An estimate of the present level of precision of The Open University system is provided by 40 analyses of an internal obsidian standard

undertaken during six separate sessions by Greenwood et al. (2015), which gave the following combined results: $\pm 0.052\text{‰}$ for $\delta^{17}\text{O}$; $\pm 0.093\text{‰}$ for $\delta^{18}\text{O}$; $\pm 0.017\text{‰}$ for $\Delta^{17}\text{O}$ (2σ). The precision (2σ) quoted for individual meteorite samples is based on replicate analyses.

Oxygen isotopic analyses are reported in standard δ notation, where $\delta^{18}\text{O}$ has been calculated as:

$$\delta^{18}\text{O} = \left[\left(\frac{{}^{18}\text{O}/{}^{16}\text{O}}{\text{sample}} / \left(\frac{{}^{18}\text{O}/{}^{16}\text{O}}{\text{ref}} \right) - 1 \right] \times 1000 \text{ (‰)}$$

$$\delta^{17}\text{O} = \left[\left(\frac{{}^{17}\text{O}/{}^{16}\text{O}}{\text{sample}} / \left(\frac{{}^{17}\text{O}/{}^{16}\text{O}}{\text{ref}} \right) - 1 \right] \times 1000 \text{ (‰)}$$

The reference being VSMOW: Vienna Standard Mean Ocean Water. $\Delta^{17}\text{O}$, which represents the deviation from the terrestrial fractionation line (TFL), has been calculated using the linearized format of Miller (2002):

$$\Delta^{17}\text{O} = 1000 \ln(1 + \delta^{17}\text{O}/1000) - \lambda 1000 \ln(1 + \delta^{18}\text{O}/1000)$$

where $\lambda = 0.5247$ (Miller, 2002; Miller et al., 1999).

RESULTS AND DISCUSSION

Mineralogy and Petrology

Hand specimen observations of a fragment of the sample highlight a fine-grained light-gray rock with some additional lighter, coarser grains present. The specimen also shows evidence of schlieren—irregular streaks with a different composition to surrounding material (Glazner et al., 2020; Figure 1). Parts of the sample appear to be stained an orange color whilst other regions appear to be rusted. XRD spectra of TJB-001, TJB-002, and TJB-003 (taken from the rusted, orange-stained, and fresh surfaces, respectively) are very similar and show diffraction peaks from plagioclase, pyroxene, and quartz (Figure S5). Based on the intensity of the peaks, the abundance of each phase probably varies slightly between the samples. No minor peaks or scattering from poorly crystalline weathering products such as rusts were observed in the XRD spectra. While their overall TGA mass loss was negligible, however, both TJB-001 (“rust”) and TJB-003 (“fresh”) showed minor (~ 1 – 2 and < 1 wt%, respectively) mass loss events at ~ 350 – 400°C that were consistent with the dehydration of “rusts” such as goethite (King et al., 2015; Figure S6). TJB-002 (“orange-stained”) differed from the other samples in having a small but distinct mass loss event (< 1 wt%) at $\sim 600^\circ\text{C}$ that could be related to the breakdown of terrestrial carbonates (e.g., Garenne et al., 2014; King et al., 2015). The fusion crust displays small regmaglypts and some abrasion as well as heterogeneity, with some regions displaying more shiny

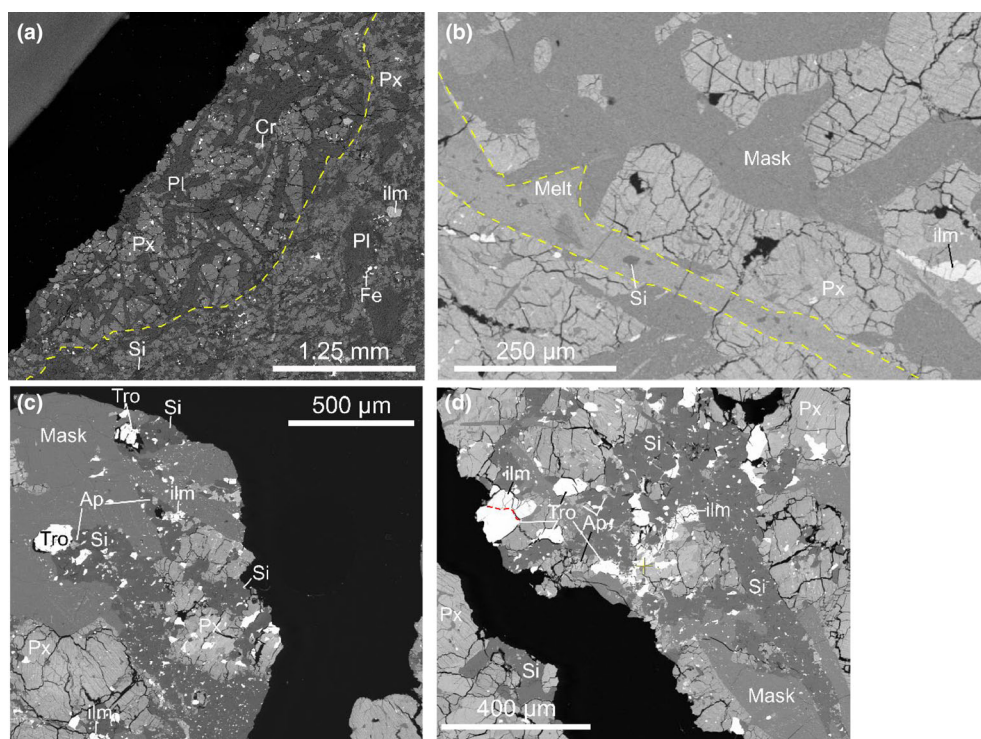


FIGURE 2. Backscattered electron (BSE) image of Padvarninkai. (a) BSE image depicting the change between a coarse-grained region and the finer-grained region divided by the yellow dotted line. (b) BSE image of a melt vein, outlined in a dotted yellow line, in a coarse-grained region. (c, d) Higher magnification BSE images of Padvarninkai; the dotted red line highlights the boundary between two bright phases, ilmenite and troilite. Ap, apatite; Cr, chromite; Fe, iron metal phase; ilm, ilmenite; Mask, maskelynite; Px, pyroxene; Pl, plagioclase; Si, Silica phase; Tro, troilite. (Color figure can be viewed at wileyonlinelibrary.com)

and glassy textures and others more crystalline (Figure 1). On one face an irregular ripple pattern can be observed in the fusion crust. Contraction cracks can also be seen, with some showing preferential oxidation within them turning these into weathering cracks. Rusting of the fusion crust is also present.

Padvarninkai is a monomict eucrite consisting of fine- to coarse-grained lithology and impact melt veins (Figure 2). Miyahara et al. (2021) highlight that some portions of Padvarninkai are unbrecciated whilst other regions display some brecciation and are more commonly associated with the melt veins. Of the thin sections studied here, the Smithsonian section appears unbrecciated whilst the new thin sections (Vilnius 1 and 2) appear more brecciated with a crystalline groundmass (see supplementary figures). The modal mineralogy (Table 1) mainly comprises low-Ca pyroxene (34.3%), high-Ca pyroxene (11.7%), plagioclase (40.6%), and a silica phase (both quartz and tridymite, 10.9%). Minor phases include ilmenite and chromite (combined oxide modal abundance 2.1%), melt (0.3%), troilite (trace), phosphates (fluorapatite and merrillite, both of which are trace), and zircon and baddeleyite (both trace). Additional minor phases observed by transmission electron microscopy by Miyahara et al.

(2021), such as majorite-bearing garnet, were not observed. The presence of both quartz and tridymite was confirmed by Raman spectroscopy (Figure S7). Quartz is a relatively rare silica phase for eucrites, which usually contain solely tridymite, and the modal abundance observed here for the combined silica phase is also high for typical eucrite silica phase modal abundances (1.1%–7.7%; Delaney et al., 1984 referenced in; Mittlefehldt, 2015), but closer to the anomalous eucrite Emmaville which also contains quartz (8.9%; Barrett et al., 2017). As both tridymite and quartz are observed within Padvarninkai, it suggests that either: (1) tridymite converted to quartz owing to an increase in pressure (possibly through shock e.g., Zamiatina et al., 2023), or (2) quartz converted to tridymite through an increase in temperature, possibly during the widespread metamorphism experienced by the majority of eucrites (Yamaguchi et al., 2009) (see Figure S9). Within the Smithsonian section of Padvarninkai (USMN 5946), all silica observed was quartz and displayed fracturing and a replacement texture. In the other two sections (Vil-1, Vil-2), both quartz and tridymite were observed with large grains typically tridymite and groundmass silica quartz. This would support the former hypothesis that tridymite is

TABLE 2. Average major mineral compositions for Padvarninkai. Pyroxene values normalized to six oxygen whilst plagioclase is normalized to eight.

wt%	Pyroxene		Plagioclase	
	Low-Ca <i>n</i> = 117	High-Ca <i>n</i> = 27	wt%	<i>n</i> = 93
SiO ₂	49.8	50.9	SiO ₂	45.4
TiO ₂	0.2	0.4	Al ₂ O ₃	34.6
Al ₂ O ₃	0.2	0.7	FeO	0.3
Cr ₂ O ₃	0.2	0.3	MgO	0.01
FeO	31.5	17.5	CaO	17.9
MnO	1.2	0.6	Na ₂ O	1.3
MgO	12.6	10.8	K ₂ O	0.1
CaO	3.6	18.2	Total	99.6
Total	99.4	99.5	An %	88.4
Fe/Mn	26.1	26.7	Ab %	11.2
Fe/Mg	1.4	0.9	Or %	0.4
Mg# (mol%)	41.7	52.5	Si	2.10
Wo %	7.8	38.8	Al	1.89
En %	38.4	32.1	Fe	0.01
Fs %	53.7	29.1	Mg	0.00
Si	1.98	1.97	Ca	0.89
Ti	0.01	0.01	Na	0.11
Al	0.01	0.03	K	0.00
Cr	0.01	0.01	Total	5.01
Fe	1.05	0.57		
Mn	0.04	0.02		
Mg	0.75	0.63		
Ca	0.15	0.76		
Total	4.00	4.00		

transforming into quartz owing to shock. Without knowing the specific phase of quartz (α or β), the exact nature of this transformation, however, remains ambiguous. Melt veins are observed with widths varying from ~ 16 to $73 \mu\text{m}$ (Figure 2b), significantly smaller than those observed by Miyahara et al. (2021) (0.6–6.6 mm), along with large mesostasis pockets which display a granoblastic texture. Average major element mineral compositions are given in Table 2.

Pyroxene and plagioclase grains are typically ~ 10 – $60 \mu\text{m}$ in the longest direction; however, some regions are noticeably coarser with grains up to $\sim 500 \mu\text{m}$ in the longest direction. Large clasts of both minerals can be found up to 2.1 and 2.3 mm, respectively. Pyroxenes are pigeonite (low-Ca host $\text{En}_{38}\text{Fs}_{54}\text{Wo}_8$; Mg# 41.7) in composition, and based on their characteristics, Padvarninkai can be considered a type 5 eucrite (based on the thermal metamorphism scale of Takeda & Graham, 1991). The pyroxene grains are severely fractured and mosaicked, and despite the shock features observed, the igneous texture is still well preserved with pyroxene displaying exsolution lamellae at a variety of scales (lamellae are 6– $22 \mu\text{m}$ width;

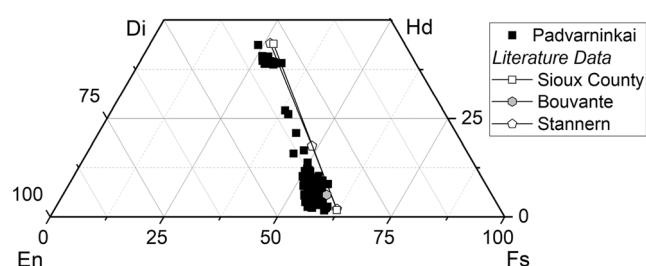


FIGURE 3. Truncated pyroxene ternary of Padvarninkai data. Literature eucrite data is taken from table S2 of Mittlefehldt (2015) and references therein.

$\text{En}_{32}\text{Fs}_{29}\text{Wo}_{39}$; Mg# 52.5; Figures 2 and 3). These Mg# values are slightly higher than the eucrite average suggesting the presence of more magnesian pyroxene values (Low-Ca pyroxene average Mg# 39.55, based on a combination of orthopyroxene and pigeonite; orthopyroxene average 38.93, pigeonite average 40.09, augite average 50.07; data from supplementary material of Mittlefehldt, 2015 and references therein). Figure 4 shows that the Fe/Mn ratio of Padvarninkai pyroxene falls toward the lower end (i.e., low but within 2SD of the basaltic eucrite Fe/Mn mean) of the normal range of basaltic eucrites. Plagioclase ($\text{An}_{88}\text{Ab}_{11}\text{Or}_{0.4}$) is mostly ophitic in texture and, depending on the grain's proximity to impact melt veins, either partially or totally converted to maskelynite. Apatite (~ 50 – $100 \mu\text{m}$ in the longest direction) are fluorine rich, subhedral to anhedral, and heavily fractured (Table 3; Figure 5).

Shock Features

Previous studies have suggested that Padvarninkai is one of, if not the, most shocked eucrite currently known within our collection, with initial estimates from 42 to 60 GPa (Yamaguchi et al., 1993). Kunz et al. (1997) initially noted some shock heterogeneity in Padvarninkai, with the sample displaying a melt matrix with embedded highly shocked clasts where plagioclase has converted to maskelynite, a lithology less strongly shocked with unaltered plagioclase, and a minor lithology with a quenched texture that they believed formed by total melting and rapid cooling to sub-solidus temperatures. Based on the ^{40}Ar - ^{39}Ar age dates obtained by Kunz et al. (1997), these authors suggested three events affected the ^{40}Ar - ^{39}Ar chronology of the sample. More recently, Miyahara et al. (2021) described in detail the shock-melt veins and high-pressure polymorphs entrained within the shock-melt zones. They proposed two different impact events within Padvarninkai: The first impact event brecciated parts of the host rock and vitrified some mineral phases (22–27 GPa), while the second induced melting of the brecciated portion resulting in the

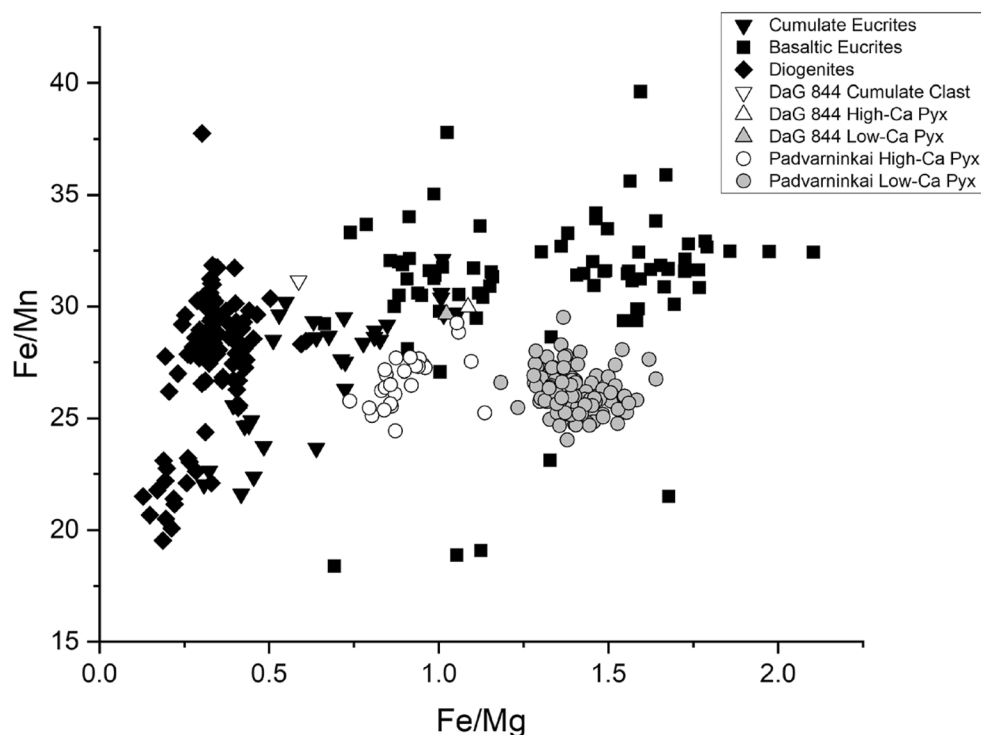


FIGURE 4. Pyroxene molar Fe/Mn versus Fe/Mg. Average data is provided for DaG 844 (see supplementary material). Basaltic eucrite, cumulate eucrite, and diogenite data are taken from the supplementary material of Mittlefehldt (2015) and references therein.

shock-melt veins at high temperature but relatively low pressure (2–13 GPa). Both of these shock estimates are significantly lower than previous estimates of 42–60 GPa (Yamaguchi et al., 1993). Two explanations for the possible reduction in shock pressure estimates are (1) plagioclase in Padvarninkai is very calcic ($An_{88.4}$ Table 2) and maskelynite formation can occur at lower pressures with increasing Ca-content (Fritz et al., 2017; Kubo et al., 2010), and (2) the pressure required for maskelynitization is lower at higher temperatures, which can allow plagioclase to transform near-melt veins at overall lower pressures (Kubo et al., 2010). It is possible that both of these factors could contribute to lower than previous shock estimates.

Observations based on the thin sections studied in this work, however, do not correlate with the lower shock estimates. Planar deformation features can be observed in both pyroxene (30–70 GPa) and plagioclase (18–34 GPa) in plane-polarized light (Stöffler et al., 2018). The shock microstructures, volatile (H and Cl) abundance, and isotopic composition of apatite in Padvarninkai were recently investigated by Barrett et al. (2021) using electron backscatter diffraction (EBSD) and nano secondary ion mass spectrometry (NanoSIMS) on a thin section also studied here (the Smithsonian section USMN 5946). EBSD maps from Barrett et al. (2021) indicate

some mosaicism of pyroxene grains surrounding the apatite. Furthermore, apatite grains in these maps reveal extensive sub-grain formation and potentially the onset of recrystallization, and a large spread in intracrystalline orientations (up to $\sim 60^\circ$), indicative of high shock. Based on the shock scale provided by Černok et al. (2019) for lunar apatite and merrillite using EBSD, apatite in Padvarninkai can be classified as S5.

Recently, Kanemaru et al. (2020) classified the bulk-rock shock effects of eucrites from A (unshocked to weakly shocked) to E (highly shocked). Given that much of the plagioclase in Padvarninkai has transformed into maskelynite, the meteorite can be assigned a rating of E (highly shocked) in agreement with the assessment by Miyahara et al. (2021). Shock stage E is consistent with shock grade S4–5 (Fritz et al., 2017; Rubin et al., 1997) and M-S4 (Stöffler et al., 2018) corresponding to an estimated equilibrium pressure that ranges from 20 to 35 GPa. Based on the features observed in apatite and pyroxene within the thin sections studied here, however, a higher shock pressure than that observed by Miyahara et al. (2021) is suggested with features more consistent with M-S4/5 (lack of vesicles in melt structures argues against solely M-S5 grading; Stöffler et al., 2018), which is at the lower end of the original pressure estimate for the sample (~ 42 GPa; Yamaguchi et al., 1993). It should

TABLE 3. Average apatite mineral composition.

Padvarninkai	
wt%	<i>n</i> = 12
P ₂ O ₅	41.89
SiO ₂	0.60
SO ₂	0.12
Y ₂ O ₃	0.02
Ce ₂ O ₃	0.02
MgO	0.03
CaO	55.48
MnO	0.01
FeO	0.74
Na ₂ O	0.01
F	3.16
F 2SD	0.29
Cl	0.12
Cl 2SD	0.05
Total	102.2
O = F + Cl	1.36
Total	100.8
P	5.902
Si	0.100
S	0.018
Y	0.002
Ce	0.001
Mg	0.007
Ca	9.890
Mn	0.002
Fe	0.103
Na	0.002
Total cations	16.028
F	1.664
Cl	0.033
Total anions	1.697
OH	0.303
Aion %	
F %	83.2
Cl %	1.6
OH %	15.1

be noted, however, that shock pressure within meteorites can be very heterogenous (e.g., Koroteev et al., 2013; Moreau et al., 2018) and it is certainly possible that the range of shock pressure estimates for Padvarninkai reflect this heterogeneity across multiple thin sections.

Bulk Rock Major, Minor, and Trace Elements

Bulk rock major element compositions are given in Table 4. For the majority of major elements analyzed here, Padvarninkai plots within the relatively narrow range of basaltic eucrite values; both P and K, however are toward the lower end of the basaltic eucrite range

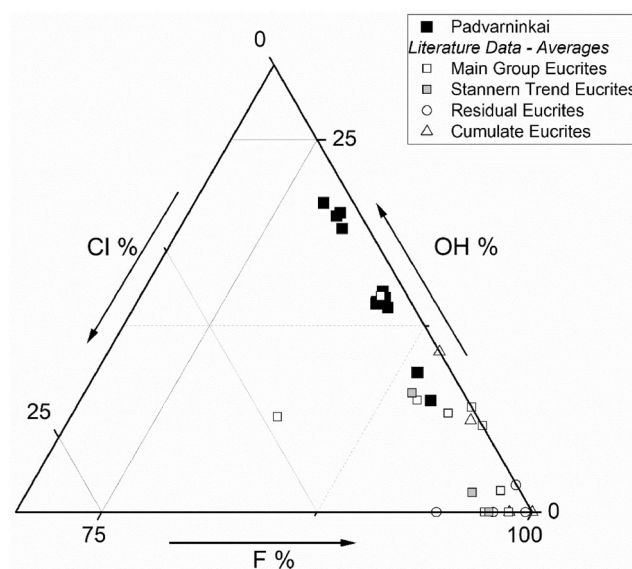


FIGURE 5. Truncated diagram of atomic proportions of F, Cl, and OH (mole%) in the X site of apatite. Average literature data taken from Sarafian et al. (2013) and Barrett et al. (2019).

TABLE 4. Bulk major element abundances. Padvarninkai A data was collected at the Natural History Museum, whilst Padvarninkai B was collected at The Open University. The “—” indicates the elements were not measured in that run. Fe₂O₃ (T) refers to total iron.

Element (wt%)	DaG 844	Padvarninkai A	Padvarninkai B
Al ₂ O ₃	10.49	12.36	—
CaO	8.87	10.36	—
Fe ₂ O ₃ (T)	19.45	20.71	—
K ₂ O	0.043	0.028	—
MgO	10.1	6.25	6.31
MnO	0.540	0.570	0.539
Na ₂ O	0.400	0.420	—
P ₂ O ₅	0.060	0.030	—
SiO ₂	50.86	49.42	—
TiO ₂	0.630	0.630	0.723
Total	101.4	100.8	—

(Figures S1 and S2; based on the bulk element data in the supplementary of Mittlefehldt, 2015 and references therein). For comparison, DaG 844 has elevated Mg, lower than average Al, as well as several elements that are within two standard deviations of the average basaltic eucrite value but close to the ends of the range (Ca low; Si high). Minor and trace element abundances are given in Table 5 and plotted in Figures 6 and 7. Compared to basaltic eucrites, both DaG 844 and Padvarninkai have high Ni contents whilst Padvarninkai also has a slightly low U content (Table 5). DaG 844 is also elevated in both Cr and Co. The overall REE patterns for Padvarninkai

TABLE 5. Bulk minor and trace element abundances. All measurements are in $\mu\text{g g}^{-1}$ (ppm) unless otherwise specified. Padvarninkai A data was collected at the Natural History Museum, whilst Padvarninkai B was collected at The Open University. The “<” indicates elements below detection limit and “—” indicates the element was not measured.

	DaG 844	Padvarninkai A	Padvarninkai B
Li	6.54	5.71	8.26
Be (ng g^{-1})	320	260	—
Sc	25.7	28.3	31.3
V	83.5	71.6	65.5
Cr (mg g^{-1})	3.35	2.50	1.92
Co	13.3	8.86	2.99
Ni	51.5	41.8	12.4
Cu	3.03	3.17	2.68
Zn	4.65	3.86	3.33
Ga	1.39	1.42	1.31
Ge (ng g^{-1})	66.4	370	—
As (ng g^{-1})	989	864	—
Rb	<	<	301
Sr	74.5	74.5	75.7
Y	16.6	14.6	17.5
Zr	58.4	43.7	43.7
Nb	4.27	3.18	3.62
Mo	<	<	10
Cd (ng g^{-1})	11	10	12
Sn (ng g^{-1})	<	279	—
Sb (ng g^{-1})	7.20	25.3	6.00
Cs	<	<	13
Ba	38.4	26.5	29.7
La	3.77	2.62	2.59
Ce	9.56	6.93	6.83
Pr	1.39	1.03	1.07
Nd	7.05	5.25	5.26
Sm	2.16	1.68	1.75
Eu	0.63	0.64	0.62
Gd	3.00	2.43	2.33
Tb	0.52	0.44	0.43
Dy	3.25	2.80	2.88
Ho	0.72	0.63	0.64
Er	1.98	1.80	1.84
Tm	0.30	0.28	—
Yb	1.96	1.85	1.69
Lu	0.29	0.28	0.27
Hf	1.67	1.32	1.13
Ta (ng g^{-1})	259	194	303
W (ng g^{-1})	296	<	88
Re (ng g^{-1})	<	<	—
Tl (ng g^{-1})	<	<	<
Pb (ng g^{-1})	560	330	312
Th (ng g^{-1})	459	327	341
U (ng g^{-1})	132	85	123

and DaG 844 are flat ($\sim 10.5\text{--}12\times\text{CI}$) similar to other basaltic eucrites and are clearly resolvable from the Stannern trend (Figure 6). As such, both Padvarninkai and DaG 844 can be considered part of the Main Group of eucrites geochemically.

The bulk rock data for Padvarninkai presented (Tables 4 and 5) here expand upon, and are broadly consistent with, the small amount of published literature on the sample (see the supplementary data for a comparison of literature values to this dataset; Barrat et al., 2000; Mason et al., 1979; Mittlefehldt & Lindstrom, 2003; Urey & Craig, 1953). Some elements, however, do show some variation compared to the literature. With regard to major elements, both Si and Mn are elevated but still within the error of the average values. In terms of minor and trace elements, Cr and Th are both elevated whilst Ba and Sr are depleted (Table 5). All these elements, however, are within error of the literature average with only U being outside of the Padvarninkai average. It should again be noted that, given the small amount of data available for this sample, the observed elevations/depletions could reflect the natural variation within Padvarninkai. When comparing the different aliquot data measured independently at two laboratories, the majority of major, minor, and trace elements are in close agreement with each other (see supplementary material). This agreement between results would argue against analytical artifacts such as contamination, incomplete digestion, or systematic measurement errors. As such, it is more likely that, owing to the heavily brecciated and highly shocked nature of Padvarninkai, the differences in Ni and Co are from heterogeneous amounts of impactor material within each aliquot (Figure S3). Despite the Ni and Co difference (41.8 ppm in one and 12.4 ppm in the other), the Ni/Co ratio for each aliquot is similar (Chondrite normalized $(\text{Ni}/\text{Co})_{\text{N}}$ of 0.221 and 0.195; Dhaliwal et al., 2023).

The Ni abundance of Padvarninkai is similar to polymict eucrites (Figure S3). This could imply that Padvarninkai has undergone some impact mixing given that high Ni content can be linked to impact contamination (e.g., Dhaliwal et al., 2023); however, based on the petrography and element maps conducted on the sections and melt veins studied here, no evidence of exogenous material is found. To properly eliminate the possibility of impactor contamination, the percentage of impactor material needed to elevate a typical eucrite to the Ni values observed in this study was modeled (C and O isotopic modeling is discussed later in this work). Average Ni contents of chondrite groups (12,393 and 13,794 ppm) were

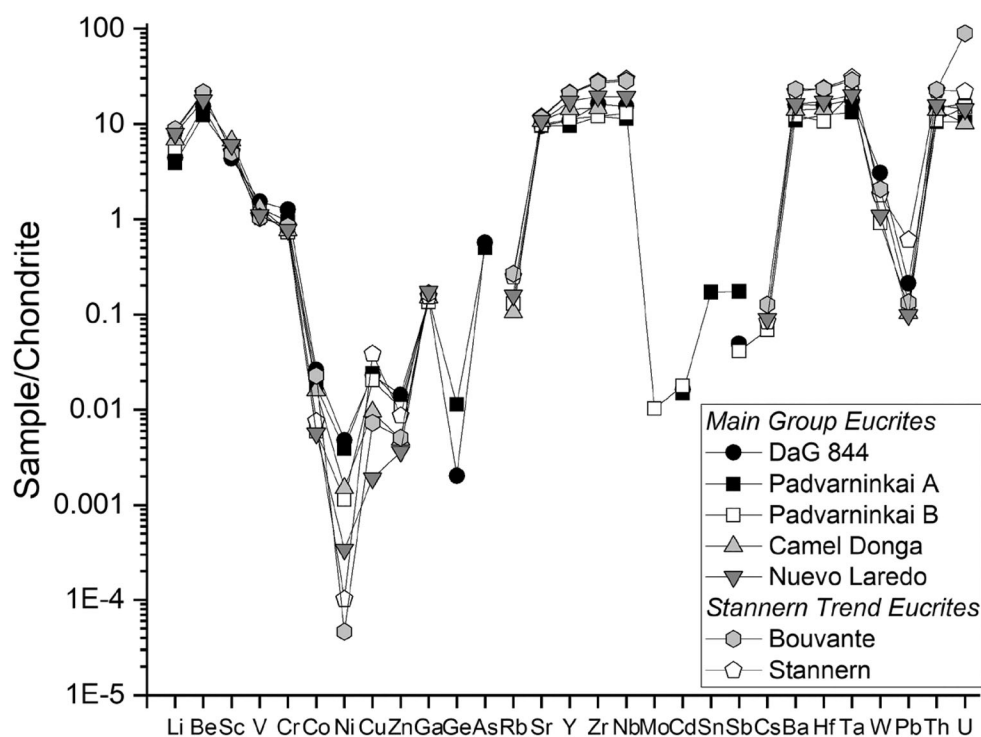


FIGURE 6. Minor element pattern of Padvarninkai and DaG 844 along with representative eucrites. Padvarninkai A represents data from the Natural History Museum, whereas B is data from The Open University. Data for Camel Donga are taken from Barrett et al. (2017). The ordering of minor elements is based on atomic number. Published values for Nuevo Laredo and Stannern are from Barrat et al. (2007). Data for Bouvante is averaged from the three sample splits also by Barrat et al. (2007). Where the authors believe the Bouvante data is of low-quality (typically split a), the data was removed from the average. The reference chondrite is from Lodders et al. (2009).

taken from Tagle and Berlin (2008), and a Ni content of 2.3 ppm, which represents a pristine noncumulate eucrite, was used as the starting eucrite component (Warren et al., 2009). It was found that <0.5% chondrite material was required across nearly all chondrite groups (LL 0.51%) to elevate Ni to comparable levels. To reconcile the isotopic compositions, however, requires significantly higher levels of mixing (as discussed in more detail below) and would result in orders of magnitude more Ni than is observed here. This further strengthens the conclusion that Padvarninkai has not had a significant impact on contamination; therefore, the elevated value may well reflect indigenous variation within Vesta. In the case of DaG 844, with a higher Ni and Co content, impact contamination is likely; however, DaG 844 does not have O-isotope data available, so it is not possible to provide a firm conclusion.

Another sample with relatively elevated Ni content is the eucrite Camel Donga (38.1 and 37.6 ppm; Barrat et al., 2000, 2007, respectively) which is known to contain a high metal content (Palme et al., 1988). Padvarninkai, however, has an even higher Ni content compared to Camel Donga (41.8 ppm) and does not contain a significant metal content in which Ni would likely be sequestered. Padvarninkai has been found to be slightly

older than, although within error of, peak basaltic magmatism on Vesta (4552 ± 7 Ma; Zhou et al., 2013) and within error, albeit at the extreme ends, of the expected core–mantle differentiation event (4564 ± 2 Ma; Zhou et al., 2013). The older age of Padvarninkai could allow for more Ni to be present during the formation of Padvarninkai. This is, however, unlikely to be the cause for the higher Ni content given the rapid core formation of Vesta effectively removing the majority of highly siderophile elements very efficiently (Dale et al., 2012; Warren et al., 2009). Partial melting models (based on those conducted by McSween et al., 2011) in equilibrium with metal (Figure S3b) are also incapable of creating Padvarninkai or any of the basaltic eucrite compositions.

Carbon and Nitrogen Isotopes

The carbon release results are shown in Figure 8. In the majority of steps, insufficient carbon was released to confidently state a release above blank level. The exception is a large release (~ 650 ng, 37.5 ppm) found at 600°C.

A 600°C release fits within the range of carbonate release temperatures during stepped combustion as defined by Grady et al. (2004). Isotopically the results are

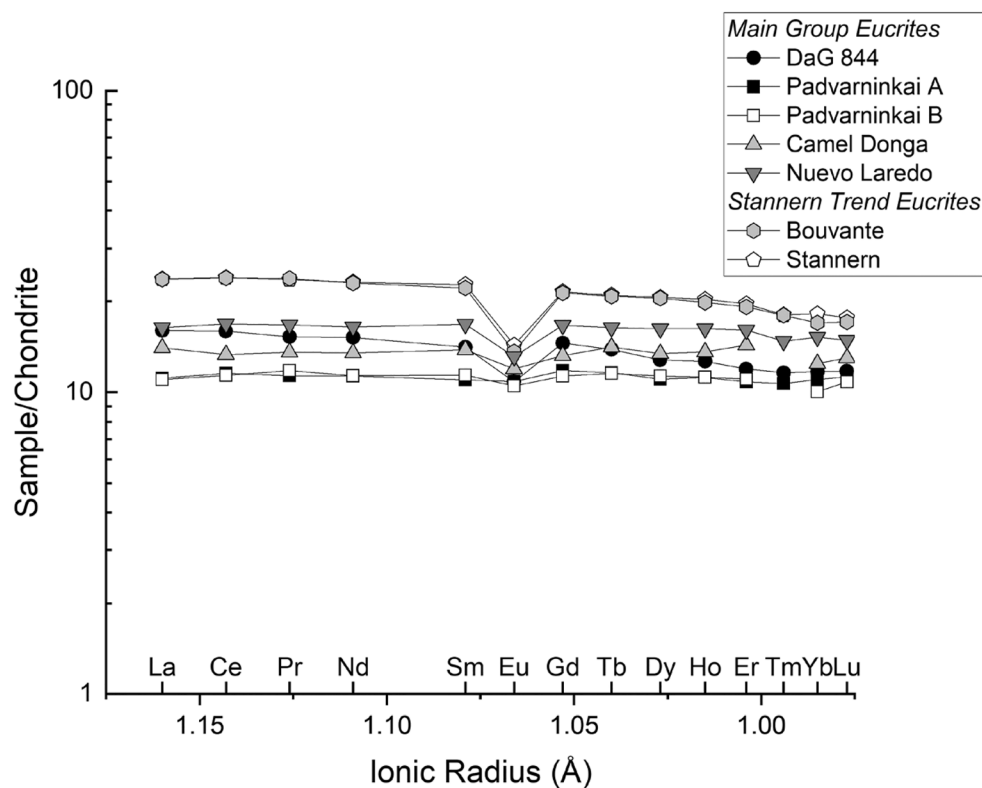


FIGURE 7. REE pattern of Padvarninkai and DaG 844 along with representative eucrites. Split A is data collected by the Natural History Museum, whilst B is data from The Open University. Data for Camel Donga are taken from Barrett et al. (2017). Published values for Nuevo Laredo and Stannern are from Barrat et al. (2007). Data for Bouvante is averaged from the three sample splits also by Barrat et al. (2007). Thulium data for Stannern and Bouvante are from Barrat et al. (2016). The reference chondrite is from Barrat et al. (2012).

suggestive of a combination of contributions from the source of the main release peak and the composition of the background ($\delta^{13}\text{C} \sim -25\%$), meaning that the minor releases below and above the main peak temperature are likely to represent oxidation of more loosely bound material and a tail from the main release, respectively. The isotopic composition of the main release, at $\delta^{13}\text{C} -5.9 \pm 2.0\%$, is within the terrestrial soil carbonate $\delta^{13}\text{C}$ range of -10% to $+5\%$ (Cerling, 1984; Cerling & Quade, 1993). The abundance and isotopic composition of carbon is also outside the typical range observed for eucrites ($\sim -25\%$ and ~ 19 ppm) observed in both unbrecciated and brecciated eucrite samples (Abernethy et al., 2018; Grady et al., 1997); however, the isotopic composition is similar to the howardite Kapoeta (-6%), albeit with approximately one-third of the C abundance (37.5 ppm compared to 94 ppm; Grady et al., 1997). Grady et al. (1997) suggested that Kapoeta could have been contaminated with CM or CR chondrite material as these chondrites contain between 100 and 2500 ppm C as carbonate, with $\delta^{13}\text{C} \sim +20$ – 80% (Alexander et al., 2015; Grady et al., 1988). CM and CR are also the most commonly found chondritic clasts in HED material

(Gounelle et al., 2003; Zolensky et al., 1996). As Padvarninkai has experienced significant impact deformation, it is possible that impact contamination, like that observed in Kapoeta, could be present within this rock. To test the Grady et al. (1997) hypothesis, the percentage of impactor material required to elevate a typical eucrite ($\delta^{13}\text{C} \sim -25\%$) to the $\delta^{13}\text{C}$ observed in this study was modeled for both CM and CR chondrites. For this model, the minimum and maximum $\delta^{13}\text{C}$ values for both heated and unheated CM and CR chondrites (based on the divisions outlined in Alexander et al., 2012, 2013) were taken from Alexander et al. (2015) and the average oxygen isotope value for these groups and eucrites was from Greenwood et al. (2017). It was found that for unheated CM and CR chondrites, using the minimum values, the percentage required to elevate the $\delta^{13}\text{C}$ values was 36% and 34%, respectively. Using the maximum $\delta^{13}\text{C}$ values requires significantly less contaminant at 19.5% and 18.5% CM and CR, respectively. Heated chondrites required significantly more contamination to achieve the required $\delta^{13}\text{C}$ value of Padvarninkai ($>70\%$ using minimum values and 20%–24% using maximum). None of these models for carbon

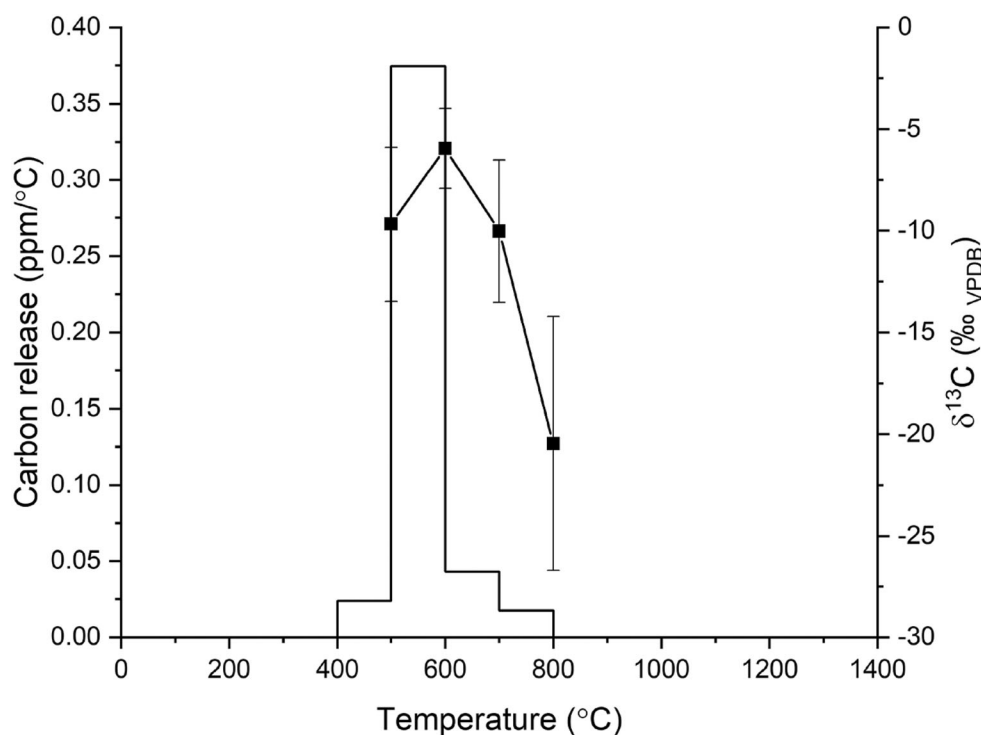


FIGURE 8. Step plot of the Padvarninkai carbon results. Abundance for each step is shown on the left Y-axis, normalized to release per degree and relating to the histogram. Isotopic results are shown on the right Y-axis.

can be reconciled with oxygen isotopes, however, which necessitates >10% CM material. Mixing of CR chondrites with lighter $\delta^{18}\text{O}$ than eucrites gives the opposite trend to that required and, therefore, cannot be a candidate for the impactor. Models also cannot reconcile the $\Delta^{17}\text{O}$ values for Padvarninkai. Mixing of ordinary chondrites additionally can be ruled out for similar reasons as neither carbon nor oxygen isotopes can explain the Ni content, although C isotope data for ordinary chondrites is limited (see Grady & Wright, 2003).

When combined with the modeling of Ni (see earlier section), it would appear that impact contamination cannot easily reconcile the Ni and $\delta^{13}\text{C}$ values with the $\delta^{18}\text{O}$ value of Padvarninkai. Based on these simple models and the lack of observed exogenous material, it is unlikely that Padvarninkai records impact contamination and these elevated signatures are either primary or caused by a different mechanism (e.g., terrestrial contamination for carbon).

Interestingly, the potential terrestrial alteration identified in TGA, which may be the cause of the heavier than normal $\delta^{13}\text{C}$ values, does not appear to have affected other isotopic compositions (Greenwood et al., 2005 and this study for O isotopes; Barrett et al., 2021 for H and Cl isotopes). Given the carbon-poor nature of the eucrites, only a small amount of material would be required to contaminate the

carbon measurements compared to other isotopic systems with higher indigenous abundances. As such, neither terrestrial contamination nor impact contamination of non-chondritic material can be fully ruled out as a cause of the anomalous $\delta^{13}\text{C}$, carbon-rich values observed within Padvarninkai.

Nitrogen results did not exceed blank level by any meaningful level.

Oxygen Isotopes

Oxygen isotope results are given in Table 6 and plotted in Figure 9. Reanalyzed replicates of Padvarninkai from the same material as Greenwood et al. (2017) are within 2σ uncertainty of each other and have similar 2σ uncertainties, with this dataset combining more analyses into each replicate ($n=4$; as opposed to $n=2$). The fractions taken from the hand specimen (Figure 1), however, display significant variation in $\delta^{18}\text{O}$ values but are typically within the HED range for $\Delta^{17}\text{O}$ values. There is also a clear difference between the EATG-washed and unwashed samples. In the case of the “fresh” and “rust” aliquots, the EATG-wash increased the $\delta^{18}\text{O}$ value and for the “rust” fraction also decreases the $\Delta^{17}\text{O}$ value (Figure 9). For the “orange” fraction, the same decrease in $\Delta^{17}\text{O}$ value is observed but there is also a decrease in the $\delta^{18}\text{O}$ value. When comparing the non-

TABLE 6. Oxygen isotope composition of Padvarninkai replicates and selected components.

Sample	<i>N</i>	$\delta^{17}\text{O}$ (‰)	2σ	$\delta^{18}\text{O}$ (‰)	2σ	$\Delta^{17}\text{O}$ (‰)	2σ	$\Delta^{17}\text{O}_{\text{linear}}$ (‰)	2σ
Replicates from same aliquot as Greenwood et al. (2017)									
Padvarninkai Replicate 1	4	1.653	0.027	3.641	0.001	-0.240	0.027	-0.255	0.027
Padvarninkai Replicate 2	4	1.739	0.021	3.769	0.013	-0.220	0.022	-0.236	0.022
Mean of two Replicates		1.696	0.122	3.705	0.181	-0.230	0.028	-0.245	0.027
Sub-fractions from hand specimen									
Fresh	4	1.444	0.049	3.228	0.020	-0.235	0.051	-0.249	0.05
Fresh EATG	4	1.704	0.032	3.731	0.009	-0.236	0.032	-0.251	0.03
Rust	4	1.683	0.061	3.681	0.017	-0.231	0.062	-0.246	0.06
Rust EATG	4	2.014	0.008	4.276	0.007	-0.210	0.009	-0.227	0.01
Orange	4	2.098	0.044	4.450	0.016	-0.216	0.049	-0.234	0.05
Orange EATG	4	1.822	0.016	3.908	0.037	-0.211	0.031	-0.227	0.03

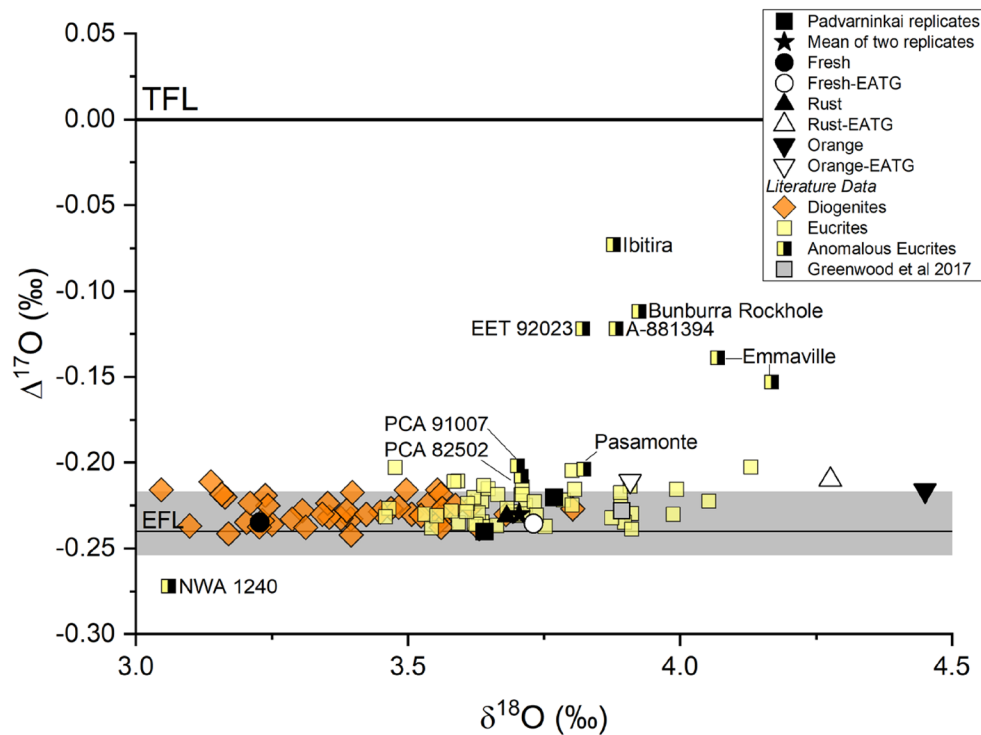


FIGURE 9. Oxygen isotope composition of Padvarninkai fractions and replicates shown in relation to other HEDs. EFL, euclite fractionation line; TFL, terrestrial fractionation line. Gray shading = HED $\Delta^{17}\text{O}$ range (Greenwood et al., 2017). Euclite and diogenite analyses are from Greenwood et al. (2017), A-881394, NWA 1240, and Pasamonte (Scott et al., 2009), Bunburra Rockhole (Bland et al., 2009), Emmaville (Barrett et al., 2017; Greenwood et al., 2017), EET 92023, Ibitira, PCA 82502 (Greenwood et al., 2017). (Color figure can be viewed at wileyonlinelibrary.com)

EATG-washed fractions, a subtle decrease $\Delta^{17}\text{O}$ value can be observed between the “fresh” (-0.235‰), “rust” (-0.231‰), and “orange” (-0.216‰) fractions. This could indicate a progressive, although very minimal, terrestrial weathering trend from “fresh” to “orange” within Padvarninkai. If this is indeed terrestrial weathering, then it would be expected that EATG would remove this component and move the $\Delta^{17}\text{O}$ values away from the TFL and closer to the euclite fractionation line (EFL). The reverse of this, however, is observed with

both the EATG-washed “rust” and “orange” fractions increasing slightly in $\Delta^{17}\text{O}$ value and plotting just outside of the HED range which could indicate the removal of primary phases (Alexander et al., 2018). Interestingly, the EATG-wash of the “fresh” sub-fraction does not significantly alter the $\Delta^{17}\text{O}$ value (a change of 0.001‰).

Given that none of the samples, EATG-washed or otherwise, plot close to the TFL and all non-EATG-washed subfractions as well as replicates from older aliquots all plot within the EFL range, this would strongly argue for

minimal terrestrial contamination especially when coupled with the minimal alteration observed in TGA and XRD.

SUMMARY

The results presented here provide a comprehensive examination of the petrology; mineral composition; bulk rock major, minor, and trace element abundances; and isotopic composition (C, O) of the Padvarninkai meteorite fall. Texturally, Padvarninkai is a highly shocked eucrite; however, it does retain some of its original igneous textures. Features observed in this sample are indicative of a shock grade of M-S4/5, suggestive of shock pressures lower than originally suggested (Yamaguchi et al., 1993) but higher than those of recent analyses (Miyahara et al., 2021). Compositionally, it is a main group basaltic eucrite, and the observed deviations from the basaltic eucrite average are likely primary and unlikely to be the result of impact contamination. Isotopically, the sample has anomalously high $\delta^{13}\text{C}$ values although oxygen and other volatile isotope systems are not altered, which argues against a terrestrial or impact contaminant cause. As Padvarninkai has such low carbon content, however, it is not possible to definitively conclude.

Given the monomict nature and ancient age of Padvarninkai, further analysis of this sample has the potential to provide important additional insights into the reservoirs and processes prevalent early in Vesta's history and if/how these could have been affected by the significant shock pressures this sample has experienced.

Acknowledgments—The following institutions are thanked for providing samples for this research: Vilnius University Department of Geology and Mineralogy and the Smithsonian Institute (USNM 5946). Andy Tindle is thanked for hand specimen photography of Padvarninkai. David 'Duck' Mittlefehldt is also thanked for their comments on the manuscript. The reviewer Jean-Alix Barrat and an anonymous reviewer along with the editor-in-chief Timothy Jull are thanked for their insightful feedback, suggestions, and comments. TJB acknowledges support through the Space Strategic Research Area (Space SRA) funding at The Open University. AJK is funded by UK Research and Innovation (UKRI) through grant number MR/T020261/1. MA acknowledge funding from STFC grants #ST/T000228/1 and ST/X001180/1. A small amount of additional time for TJB was provided by the NASA Solar System Exploration Research Virtual Institute (SSERVI) through a cooperative agreement (80NSSC20M0016, PI David A. Kring) with the USRA at the LPI in a collaboration between our SSERVI team and an SSERVI international partner. LPI contribution number (3069).

Data Availability Statement—The data that support the findings of this study are available in the supplementary material of this article.

Editorial Handling—Dr. Akira Yamaguchi

REFERENCES

- Abernethy, F. A. J., Verchovsky, A. B., Franchi, I. A., and Grady, M. M. 2018. Basaltic Volcanism on the Angrite Parent Body: Comparison with 4 Vesta. *Meteoritics & Planetary Science* 53: 375–393.
- Alexander, C. M. O'D., Bowden, R., Fogel, M. L., and Howard, K. T. 2015. Carbonate Abundances and Isotopic Compositions in Chondrites. *Meteoritics & Planetary Science* 50: 810–833.
- Alexander, C. M. O'D., Bowden, R., Fogel, M. L., Howard, K. T., Herd, C. D. K., and Nittler, L. R. 2012. The Provenances of Asteroids, and Their Contributions to the Volatile Inventories of the Terrestrial Planets. *Science* 337: 721–23.
- Alexander, C. M. O'D., Greenwood, R. C., Bowden, R., Gibson, J. M., Howard, K. T., and Franchi, I. A. 2018. A Multi-Technique Search for the most Primitive CO Chondrites. *Geochimica et Cosmochimica Acta* 221: 406–420.
- Alexander, C. M. O'D., Howard, K. T., Bowden, R., and Fogel, M. L. 2013. The Classification of CM and CR Chondrites Using Bulk H, C and N Abundances and Isotopic Compositions. *Geochimica et Cosmochimica Acta* 123: 244–260.
- B.V.S.P. 1981. *Basaltic Volcanism on the Terrestrial Planets*. New York: Pergamon Press, Inc.
- Barrat, J.-A., Blichert-Toft, J., Gillet, P., and Keller, F. 2000. The Differentiation of Eucrites: The Role of In Situ Crystallization. *Meteoritics & Planetary Science* 35: 1087–1100.
- Barrat, J. A., Dauphas, N., Gillet, P., Bollinger, C., Etoubleau, J., Bischoff, A., and Yamaguchi, A. 2016. Evidence From Tm anomalies for Non-CI Refractory Lithophile Element Proportions in Terrestrial Planets and Achondrites. *Geochimica et Cosmochimica Acta* 176: 1–17.
- Barrat, J. A., Zanda, B., Moynier, F., Bollinger, C., Liorzou, C., and Bayon, G. 2012. Geochemistry of CI Chondrites: Major and Trace Elements, and Cu and Zn Isotopes. *Geochimica et Cosmochimica Acta* 83: 79–92.
- Barrat, J.-A., Yamaguchi, A., Greenwood, R., Bohn, M., Cotten, J., Benoit, M., and Franchi, I. 2007. The Stannern Trend Eucrites: Contamination of Main Group Eucritic Magmas by Crustal Partial Melts. *Geochimica et Cosmochimica Acta* 71: 4108–24.
- Barrett, T. J., Barnes, J. J., Anand, M., Franchi, I. A., Greenwood, R. C., Charlier, B. L. A., Zhao, X., Moynier, F., and Grady, M. M. 2019. Investigating Magmatic Processes in the Early Solar System Using the Cl Isotopic Systematics of Eucrites. *Geochimica et Cosmochimica Acta* 266: 582–597.
- Barrett, T. J., Černok, A., Degli-Alessandrini, G., Zhao, X., Anand, M., Franchi, I. A., and Darling, J. R. 2021. Exploring Relationships between Shock-Induced Microstructures and H₂O and Cl in Apatite Grains from Eucrite Meteorites. *Geochimica et Cosmochimica Acta* 302: 120–140.

- Barrett, T. J., Mittlefehldt, D. W., Greenwood, R. C., Charlier, B. L. A., Hammond, S. J., Ross, D. K., Anand, M., Franchi, I. A., Abernethy, F. A. J., and Grady, M. M. 2017. The Mineralogy, Petrology, and Composition of Anomalous Euclite Emmaville. *Meteoritics & Planetary Science* 52: 656–668.
- Binns, R. A. 1967. Stony Meteorites Bearing Maskelynite. *Nature* 213: 1111–12.
- Bischoff, A., and Stöfler, D. 1992. Shock Metamorphism as a Fundamental Process in the Evolution of Planetary Bodies: Information from Meteorites. *European Journal of Mineralogy* 4: 707–755.
- Bland, P. A., Spurný, P., Towner, M. C., Bevan, A. W. R., Singleton, A. T., Bottke, W. F., Greenwood, R. C., et al. 2009. An Anomalous Basaltic Meteorite from the Innermost Main Belt. *Science* 325: 1525–27.
- Bukovanská, M., Ireland, T., and Janicke, J. 1997. Zircons and Baddeleyites from Differentiated Meteorites—Basaltic Achondrites: Ion Probe Dating and REE Systematics. *Journal of Geosciences* 42: 20.
- Cerling, T. E. 1984. The Stable Isotopic Composition of Modern Soil Carbonate and its Relationship to Climate. *Earth and Planetary Science Letters* 71: 229–240.
- Cerling, T. E., and Quade, J. 1993. Stable Carbon and Oxygen Isotopes in Soil Carbonates. In *Climate Change in Continental Isotopic Records. Geophysical Monograph*, edited by P. K. Swart, K. C. Lohmann, J. Mckenzie, and S. Savin, vol. 78, 217–231. Washington, D.C.: AGU.
- Černok, A., White, L. F., Darling, J., Dunlop, J., and Anand, M. 2019. Shock-Induced Microtextures in Lunar Apatite and Merrillite. *Meteoritics & Planetary Science* 54: 1262–82.
- Dale, C. W., Burton, K. W., Greenwood, R. C., Gannoun, A., Wade, J., Wood, B. J., and Pearson, D. G. 2012. Late Accretion on the Earliest Planetesimals Revealed by the Highly Siderophile Elements. *Science* 336: 72–75.
- De Sanctis, M. C., Ammannito, E., Capria, M. T., Capaccioni, F., Combe, J.-P., Frigeri, A., Longobardo, A., et al. 2013. Vesta's Mineralogical Composition as Revealed by the Visible and Infrared Spectrometer on Dawn. *Meteoritics & Planetary Science* 48: 2166–84.
- De Sanctis, M. C., Ammannito, E., Capria, M. T., Tosi, F., Capaccioni, F., Zambon, F., Carraro, F., et al. 2012. Spectroscopic Characterization of Mineralogy and its Diversity across Vesta. *Science* 336: 697–700.
- Delaney, J., Prinz, M., Nehru, C., and Stokes, C. 1984. Allan Hills A81001, Cumulate Euclites and Black Clasts from Polymict Euclites. *14th Lunar and Planetary Science Conference*, pp. 212–13.
- Dhaliwal, J. K., Day, J. M. D., and Tait, K. T. 2023. Pristinity and Petrogenesis of Euclites. *Meteoritics & Planetary Science* 58: 275–295.
- Duke, M. B., and Silver, L. T. 1967. Petrology of Euclites, Howardites and Mesosiderites. *Geochimica et Cosmochimica Acta* 31: 1637–65.
- Fritz, J., Greshake, A., and Fernandes, V. A. 2017. Revising the Shock Classification of Meteorites. *Meteoritics & Planetary Science* 52: 1216–32.
- Garenne, A., Beck, P., Montes-Hernandez, G., Chiriach, R., Toche, F., Quirico, E., Bonal, L., and Schmitt, B. 2014. The Abundance and Stability of “Water” in Type 1 and 2 Carbonaceous Chondrites (CI, CM and CR). *Geochimica et Cosmochimica Acta* 137: 93–112.
- Glazner, A. F., Bartley, J. M., and Law, B. S. 2020. Immiscibility and the Origin of Ladder Structures, Mafic Layering, and Schlieren in Plutons. *Geology* 49: 86–90.
- Goldoff, B., Webster, J. D., and Harlov, D. E. 2012. Characterization of Fluor-Chlorapatites by Electron Probe Microanalysis with a Focus on Time-Dependent Intensity Variation of Halogens. *American Mineralogist* 97: 1103–15.
- Gounelle, M., Zolensky, M. E., Liou, J.-C., Bland, P. A., and Alard, O. 2003. Mineralogy of Carbonaceous Chondritic Microclasts in Howardites: Identification of C2 Fossil Micrometeorites. *Geochimica et Cosmochimica Acta* 67: 507–527.
- Grady, M., and Wright, I. 2003. Elemental and Isotopic Abundances of Carbon and Nitrogen in Meteorites. *Space Science Reviews* 106: 231–248.
- Grady, M. M., Verchovsky, A. B., and Wright, I. P. 2004. Magmatic Carbon in Martian Meteorites: Attempts to Constrain the Carbon Cycle on Mars. *International Journal of Astrobiology* 3: 117–124.
- Grady, M. M., Wright, I. P., and Pillinger, C. T. 1997. Carbon in Howardite, Euclite and Diogenite Basaltic Achondrites. *Meteoritics & Planetary Science* 32: 863–68.
- Grady, M. M., Wright, I. P., Swart, P. K., and Pillinger, C. T. 1988. The Carbon and Oxygen Isotopic Composition of Meteoritic Carbonates. *Geochimica et Cosmochimica Acta* 52: 2855–66.
- Greenwood, R. C., Barrat, J.-A., Scott, E. R. D., Haack, H., Buchanan, P. C., Franchi, I. A., Yamaguchi, A., Johnson, D., Bevan, A. W. R., and Burbine, T. H. 2015. Geochemistry and Oxygen Isotope Composition of Main-Group Pallasites and Olivine-Rich Clasts in Mesosiderites: Implications for the “Great Dunite Shortage” and HED-Mesosiderite Connection. *Geochimica et Cosmochimica Acta* 169: 115–136.
- Greenwood, R. C., Burbine, T. H., Miller, M. F., and Franchi, I. A. 2017. Melting and Differentiation of Early-Formed Asteroids: The Perspective from High Precision Oxygen Isotope Studies. *Chemie der Erde-Geochemistry* 77: 1–43.
- Greenwood, R. C., Franchi, I. A., Gibson, J. M., and Benedix, G. K. 2012. Oxygen Isotope Variation in Primitive Achondrites: The Influence of Primordial, Asteroidal and Terrestrial Processes. *Geochimica et Cosmochimica Acta* 94: 146–163.
- Greenwood, R. C., Franchi, I. A., Jambon, A., and Buchanan, P. C. 2005. Widespread Magma Oceans on Asteroidal Bodies in the Early Solar System. *Nature* 435: 916–18.
- Janots, E., Gnos, E., Hofmann, B., Greenwood, R., Franchi, I., Birmingham, K., and Netwing, V. 2012. Jiddat al Harasis 556: A Howardite Impact Melt Breccia with an H Chondrite Component. *Meteoritics & Planetary Science* 47: 1558–74.
- Kanamaru, R., Imae, N., Yamaguchi, A., Takenouchi, A., and Nishido, H. 2020. Estimation of Shock Degrees of Euclites Using X-Ray Diffraction and Petrographic Methods. *Polar Science* 26: 100605.
- King, A. J., Solomon, J. R., Schofield, P. F., and Russell, S. S. 2015. Characterising the CI and CI-Like Carbonaceous Chondrites Using Thermogravimetric Analysis and Infrared Spectroscopy. *Earth, Planets and Space* 67: 198.
- Koroteev, V., Berzin, S., Erokhin, Y. V., Ivanov, K., and Khiller, V. 2013. Composition and Structure of the Chelyabinsk Meteorite. In *Doklady Earth Sciences*, vol. 451, 839–842. Springer Nature BV.
- Kubo, T., Kimura, M., Kato, T., Nishi, M., Tominaga, A., Kikegawa, T., and Funakoshi, K.-i. 2010. Plagioclase

- Breakdown as an Indicator for Shock Conditions of Meteorites. *Nature Geoscience* 3: 41–45.
- Kunz, J., Falter, M., and Jessberger, E. K. 1997. Shocked Meteorites: Argon-40-Argon-39 Evidence for Multiple Impacts. *Meteoritics & Planetary Science* 32: 647–670.
- Lodders, K., Palme, H., and Gail, H.-P. 2009. Abundances of the Elements in the Solar System: 4 The Solar System. In *Solar System*, edited by J. E. Trümper, 712–770. Heidelberg: Springer Berlin.
- Martins, Z., Hofmann, B. A., Gnos, E., Greenwood, R. C., Verchovsky, A., Franchi, I. A., Jull, A. J. T., et al. 2007. Amino Acid Composition, Petrology, Geochemistry, ¹⁴C Terrestrial Age and Oxygen Isotopes of the Shişr 033 CR Chondrite. *Meteoritics & Planetary Science* 42: 1581–95.
- Mason, B., Jarosewich, E., and Nelen, J. A. 1979. The Pyroxene-Plagioclase Achondrites. *Smithsonian Contributions to the Earth Sciences* 22: 27–45.
- Mayne, R., McSween, H., McCoy, T., and Gale, A. 2009. Petrology of the Unbrecciated Eucrites. *Geochimica et Cosmochimica Acta* 73: 794–819.
- McSween, H. Y., Binzel, R. P., De Sanctis, M. C., Ammannito, E., Prettyman, T. H., Beck, A. W., Reddy, V., et al. 2013. Dawn; the Vesta–HED Connection; and the Geologic Context for Eucrites, Diogenites, and Howardites. *Meteoritics & Planetary Science* 48: 2090–2104.
- McSween, H. Y., Mittlefehldt, D. W., Beck, A. W., Mayne, R. G., and McCoy, T. J. 2011. HED Meteorites and their Relationship to the Geology of Vesta and the Dawn Mission. *Space Science Reviews* 163: 141–174.
- Miller, M., Franchi, I., Sexton, A., and Pillinger, C. 1999. High-Precision $\delta^{17}\text{O}$ Isotope Measurements of Oxygen from Silicates and Other Oxides: Method and Applications. *Rapid Communications in Mass Spectrometry* 13: 1211–17.
- Miller, M. F. 2002. Isotopic Fractionation and the Quantification of ¹⁷O Anomalies in the Oxygen Three-Isotope System: An Appraisal and Geochemical Significance. *Geochimica et Cosmochimica Acta* 66: 1881–89.
- Misawa, K., Yamaguchi, A., and Kaiden, H. 2005. U-Pb and ²⁰⁷Pb–²⁰⁶Pb Ages of Zircons from Basaltic Eucrites: Implications for Early Basaltic Volcanism on the Eucrite Parent Body. *Geochimica et Cosmochimica Acta* 69: 5847–61.
- Mittlefehldt, D. W. 2005. Ibitira: A Basaltic Achondrite from a Distinct Parent Asteroid and Implications for the Dawn Mission. *Meteoritics & Planetary Science* 40: 665–677.
- Mittlefehldt, D. W. 2015. Asteroid (4) Vesta: I. The Howardite-Eucrite-Diogenite (HED) Clan of Meteorites. *Chemie der Erde-Geochemistry* 75: 155–183.
- Mittlefehldt, D. W., and Lindstrom, M. M. 2003. Geochemistry of Eucrites: Genesis of Basaltic Eucrites, and Hf and Ta as Petrogenetic Indicators for Altered Antarctic Eucrites. *Geochimica et Cosmochimica Acta* 67: 1911–34.
- Miyahara, M., Yamaguchi, A., Ohtani, E., Tomioka, N., and Kodama, Y. 2021. Complicated Pressure–Temperature Path Recorded in the Eucrite Padvarninkai. *Meteoritics & Planetary Science* 56: 1443–58.
- Moreau, J.-G., Kohout, T., and Wünnemann, K. 2018. Melting Efficiency of Troilite-Iron Assemblages in Shock-Darkening: Insight from Numerical Modeling. *Physics of the Earth and Planetary Interiors* 282: 25–38.
- Palme, H., Wlotzka, F., Spettel, B., Dreibus, G., and Weber, H. 1988. Camel Donga: A Eucrite with High Metal Content. *Meteoritics* 23: 49–57.
- Rubin, A. E., Scott, E. R. D., and Keil, K. 1997. Shock Metamorphism of Enstatite Chondrites. *Geochimica et Cosmochimica Acta* 61: 847–858.
- Sarafian, A. R., Roden, M. F., and Patiño-Douce, A. E. 2013. The Volatile Content of Vesta: Clues From Apatite in Eucrites. *Meteoritics & Planetary Science* 48: 2135–54.
- Schwenzer, S. P., Greenwood, R. C., Kelley, S. P., Ott, U., Tindle, A. G., Haubold, R., Herrmann, S., et al. 2013. Quantifying Noble Gas Contamination During Terrestrial Alteration in Martian Meteorites From Antarctica. *Meteoritics & Planetary Science* 48: 929–954.
- Scott, E. R. D., Greenwood, R. C., Franchi, I. A., and Sanders, I. S. 2009. Oxygen Isotopic Constraints on the Origin and Parent Bodies of Eucrites, Diogenites, and Howardites. *Geochimica et Cosmochimica Acta* 73: 5835–53.
- Stöfler, D., Hamann, C., and Metzler, K. 2018. Shock Metamorphism of Planetary Silicate Rocks and Sediments: Proposal for an Updated Classification System. *Meteoritics & Planetary Science* 53: 5–49.
- Tagle, R., and Berlin, J. 2008. A Database of Chondrite Analyses Including Platinum Group Elements, Ni, Co, Au, and Cr: Implications for the Identification of Chondritic Projectiles. *Meteoritics & Planetary Science* 43: 541–559.
- Takeda, H., and Graham, A. 1991. Degree of Equilibration of Eucritic Pyroxenes and Thermal Metamorphism of the Earliest Planetary Crust. *Meteoritics* 26: 129–134.
- Urey, H. C., and Craig, H. 1953. The Composition of the Stone Meteorites and the Origin of the Meteorites. *Geochimica et Cosmochimica Acta* 4: 36–82.
- Warren, P. H., Kallemeyn, G. W., Huber, H., Ulf-Møller, F., and Choe, W. 2009. Siderophile and Other Geochemical Constraints on Mixing Relationships among HED-Meteoritic Breccias. *Geochimica et Cosmochimica Acta* 73: 5918–43.
- Yamaguchi, A., Barrat, J. A., Greenwood, R. C., Shirai, N., Okamoto, C., Setoyanagi, T., Ebihara, M., Franchi, I. A., and Bohn, M. 2009. Crustal Partial Melting on Vesta: Evidence from Highly Metamorphosed Eucrites. *Geochimica et Cosmochimica Acta* 73: 7162–82.
- Yamaguchi, A., Mori, H., and Takeda, H. 1993. Mineralogy and Shock Textures in the Padvarninkai Eucrite (Abstract Presented at the 56th Annual Meeting of the Meteoritical Society). *Meteoritics* 28: 462–63.
- Zamiatina, D. A., Zamyatin, D. A., Mikhalevskii, G. B., and Chebikin, N. S. 2023. Silica Polymorphs Formation in the Jänisjärvi Impact Structure: Tridymite, Cristobalite, Quartz, Trace Stishovite and Coesite. *Minerals* 13: 686.
- Zhou, Q., Yin, Q.-Z., Young, E. D., Li, X.-H., Wu, F.-Y., Li, Q.-L., Liu, Y., and Tang, G.-Q. 2013. SIMS Pb–Pb and U–Pb Age Determination of Eucrite Zircons at <5 μm Scale and the First 50 Ma of the Thermal History of Vesta. *Geochimica et Cosmochimica Acta* 110: 152–175.
- Zolensky, M. E., Weisberg, M. K., Buchanan, P. C., and Mittlefehldt, D. W. 1996. Mineralogy of Carbonaceous Chondrite Clasts in HED Achondrites and the Moon. *Meteoritics & Planetary Science* 31: 518–537.

SUPPORTING INFORMATION

Additional supporting information may be found in the online version of this article.

Figure S1. Al versus Mg, Ti versus Mg, Na versus Mg, Ca versus Mg for Padvarninkai and DaG 844. Basaltic and polymict eucrite data is taken from the supplementary material (Table S7) of Mittlefehldt (2015) and references therein.

Figure S2. Mg versus Si, Fe versus Mg, Al versus Si, Ti versus Si for Padvarninkai and DaG 844. Basaltic and polymict eucrite data is taken from Table S7 of Mittlefehldt (2015) and references therein.

Figure S3. (a) Graph of Co versus Ni in Padvarninkai and DaG 844 with increasing Ni content a potential indication of impactor addition. (b) Co versus Ni with partial melt models representing a partial melt in equilibrium with metal. The partial melt model follows the procedure outlined in McSween et al. (2011) and references therein. Basaltic and polymict eucrite data is taken from Table S7 of Mittlefehldt (2015) and references therein. Padvarninkai A represents data from the Natural History Museum, Padvarninkai B represents data from The Open University.

Figure S4. Truncated pyroxene ternary of DaG 844 data.

Figure S5. XRD spectra for the different scrapings of Padvarninkai. TJB-001 = Rusted material, TJB-002 = ‘Orange’ altered material, TJB-003 = Fresh Padvarninkai material.

Figure S6. Left hand side—Mass loss (%) and Derivative Thermogravimetry (DTG; wt%/°C) curves for samples TJB-001, TJB-002, and TJB-003. TJB-001 and TJB-003 show mass loss events at ~350–400°C that are

likely due to the dehydration of “rusts”. TJB-002 shows a mass loss event at ~600°C attributed to the breakdown of carbonates. Right hand side—The DTG (wt%/°C) curves of TJB-001, TJB-002, and TJB-003 compared to those for terrestrial “rusts” (limonite, goethite), carbonates (calcite), and phyllosilicates (chrysotile) reported by King et al. (2015). TJB-001 = Rusted material, TJB-002 = ‘Orange’ altered material, TJB-003 = Fresh Padvarninkai material.

Figure S7. Raman spectra from (a) the Smithsonian thin section (USNM 5946), (b) and (c) are the two thin sections prepared at The Open University from the piece provided by Vilnius University Department of Geology and Mineralogy (Vil-1, Vil-2). Reference spectra are taken from the RRUFF database (R040031 and R090042 for quartz and tridymite, respectively).

Figure S8. Full section BSE maps of each of the studied thin sections. Main mineral phases include pyroxene, plagioclase, and the silica phase (tridymite/quartz). Brighter minor phases are likely chromite, ilmenite, or troilite. For grayscale variations by phase please see Figure 2 for more information.

Figure S9. The low-pressure field of the SiO₂ phase diagram (Tuttle & Bowen, 1958). As stated in the main text, given that both tridymite and quartz are observed within Padvarninkai it suggests partial/incomplete phases transformations. Either tridymite converted to quartz owing to an increase in pressure (possibly through shock e.g., Zamiatina et al., 2023), or quartz converted to tridymite through an increase in temperature, possibly through the widespread metamorphism experienced by the majority of eucrites (Yamaguchi et al., 2009).

Data S2. Supplementary data tables and standard information.